

# Generalised optical printing of photocurable metal chalcogenides

**Seongheon Baek**

Ulsan National Institute of Science and Technology

**Hyeong Woo Ban**

Ulsan National Institute of Science and Technology

**Sanggyun Jung**

Ulsan National Institute of Science and Technology (UNIST)

**Seung Hwae Heo**

Ulsan National Institute of Science and Technology

**Da Hwi Gu**

Ulsan National Institute of Science and Technology

**Wooyong Choi**

Ulsan National Institute of Science and Technology

**Seungjun Choo**

Ulsan National Institute of Science and Technology

**Yae Eun Park**

Ulsan National Institute of Science and Technology (UNIST)

**Jiseok Lee**

Ulsan National Institute of Science and Technology <https://orcid.org/0000-0003-2968-2458>

**Jae Sung Son** (✉ [jsson@unist.ac.kr](mailto:jsson@unist.ac.kr))

Ulsan National Institute of Science and Technology (UNIST) <https://orcid.org/0000-0003-3498-9761>

---

## Article

### Keywords:

**Posted Date:** April 12th, 2022

**DOI:** <https://doi.org/10.21203/rs.3.rs-1511446/v1>

**License:**   This work is licensed under a Creative Commons Attribution 4.0 International License.

[Read Full License](#)

---

**Version of Record:** A version of this preprint was published at Nature Communications on September 7th, 2022. See the published version at <https://doi.org/10.1038/s41467-022-33040-2>.

# Abstract

Optical three-dimensional (3D) printing techniques have attracted tremendous attention owing to their applicability to mask-less additive manufacturing, which enables the cost-effective and straightforward creation of patterned architectures. However, despite their potential use as alternatives to traditional lithography, the printable materials obtained from these methods are strictly limited to photocurable resins, thereby restricting the functionality of the printed objects and their application areas. Herein, we report a generalised direct optical printing technique to obtain functional metal chalcogenides via digital light processing. We developed universally applicable photocurable chalcogenidometallate inks that could be directly used to create 2D patterns or 3D architectures of various sizes and shapes. Our process is applicable to a diverse range of functional metal chalcogenides for compound semiconductors and 2D transition-metal dichalcogenides. We then demonstrated the feasibility of our technique by fabricating and evaluating a micro-scale thermoelectric generator bearing tens of patterned semiconductors. Our approach shows potential for simple and cost-effective architecturing of functional inorganic materials.

## Introduction

Material patterning is considered an essential prerequisite for fabricating electronic, optoelectronic, and energy devices<sup>1-5</sup>. Various methods, such as photolithography, imprint lithography, microcontact printing, and laser or electron-beam writing, have been developed to create high-resolution patterned structures in two-dimensional (2D) films<sup>6-11</sup>. However, these conventional manufacturing processes, which are based on mask or mould production, lithography, vacuum deposition, and lift-off, are often costly and require multi-step processes or expensive lithography equipment<sup>11,12</sup>. Furthermore, these 2D design processes are unsuitable for fabricating three-dimensional (3D) structures, which usually involve high costs and long processing times, when performed by traditional subtractive lithography. Optical 3D printing techniques, such as digital light processing (DLP) and stereolithography, have recently been regarded as simple and cost-effective patterning methods by additive manufacturing<sup>13,14</sup>. In these methods, automatically patterned digital masks produced by a simple electrical input create solid architectures directly from liquid-type resin inks following light exposure; thus, mask production, material deposition, and subsequent lift-off are unnecessary. Despite these advantages, however, optical printing processes suffer from the critical issue of limited printable materials. Only photocurable polymers or their composites with inorganic fillers are utilised as inks to ensure photocurability<sup>15-17</sup>. Thus, the use of these processes to create functional and high-performance inorganic material patterns is limited, and their applications in the electronic and energy fields are restricted. For example, the efficiency of DLP-printed thermoelectric BiSbTe materials is one order of magnitude lower than that of inorganic bulk reference materials because of the printed objects contain organic residues<sup>18</sup>. Calcination in air or oxygen can completely remove organic residues, but this process can also cause the undesirable oxidation of inorganic materials, such as metal chalcogenides.

Metal chalcogenides have attracted significant interest in various disciplines as well-defined semiconductor materials that are useful in various technological applications, such as electronics, optoelectronics, and thermoelectrics<sup>19–23</sup>. Tremendous efforts have been made to pattern metal chalcogenides using various lithographic and printing techniques<sup>24–29</sup>. For example, Wang et al. reported the direct optical lithography of a functional inorganic nanomaterial; in this work, spin-coated photocurable nanoparticle thin films were easily patterned by photolithography and subsequent lift-off<sup>25</sup>. Similarly, Yang et al. developed a high-resolution optical patterning process for photocurable CdSe-based quantum dots mixed with an azide-based light-driven ligand crosslinker; in these authors' work, the dots were patterned through photolithography and subsequent lift-off<sup>26</sup>. Although these methods can provide high-resolution patterns in 2D inorganic films, they still adopt conventional multi-step processes, which present challenges within the context of process simplification and 3D printability.

Chalcogenidometallates (ChaMs) have been intensively studied as soluble semiconductor inorganics that could provide metal chalcogenide inks for various printing processes. In general, these molecular anions are composed of metallic atom centres coordinated with several chalcogens and readily form crystalline metal chalcogenide phases via thermal decomposition<sup>30–34</sup>. These unique characteristics of ChaMs render them suitable candidates as precursors for the ink-processed patterning of metal chalcogenides. Herein, we report a mask-less DLP-based printing technology to obtain organics-free inorganic metal chalcogenides with 2D and 3D architectures (Fig. 1a). We developed photocurable ChaM-based inorganic inks with the aid of a photoacid generator (PAG), which enables the fabrication of complex 2D-patterned metal chalcogenides with excellent fidelity and size and shape uniformity as well as 3D architectures by 2D layer-by-layer additive manufacturing. This process was demonstrated to be universally applicable to the diverse metal chalcogenides of functional compound semiconductors and 2D layered transition metal dichalcogenides. To verify the feasibility of our proposed approach, we fabricated a micro-scale thermoelectric power generator composed of patterned SnSe<sub>2</sub> and Cu<sub>2</sub>S legs as n-type and p-type semiconductors, respectively, by DLP printing. This generator exhibited a power density of 0.564 mW cm<sup>-2</sup> under a temperature difference of 65 K. Our approach shows great potential use as a cost-effective, simple, and high-resolution direct architecturing process for inorganic materials.

## Synthesis Of Photocurable Chalcogenidometallate-based Inks

The overall process of the proposed optical printing technique using photocurable ChaM-based inks is illustrated in Fig. 1a. We used a DLP process that operates by reflecting light off microscopic mirrored panels called digital micro-mirror devices to selectively solidify the photocurable ink and create complex 3D architectures by 2D layer-by-layer curing. We synthesised diverse ranges of ChaMs containing Pt, Sb, Sn, Cu, and Mo by dissolving the corresponding metal chalcogenide powders using an ethylenediamine/ethanethiol alkahest in a N<sub>2</sub>-filled glove box or traditional coordination chemistry to generate the desired ChaM anions counterbalanced by cations of ammonium or ethylendiammonium (Fig. 1a)<sup>35,36</sup>. All ChaMs exhibited excitonic peaks in the visible range of the UV-Vis absorption spectrum due to the d–d transition or ligand-to-metal charge transfer of the metal chalcogenide complexes

(Supplementary Fig. 1)<sup>37–39</sup>. The characteristic peak at 520 nm observed in the spectra of the Sb-, Cu-, and Sn-based ChaMs originated from the alkahest solvent<sup>40</sup>.

The synthesised ChaMs were mixed with an appropriate amount of PAGs to formulate the photocurable ChaM-based inks. Here, the purification step of the ChaMs is essential to ensure their photocurability in the presence of PAGs because unreacted metal chalcogenides or by-products could negatively affect the kinetics of the photoreaction of the ChaMs. In addition, the basic reaction medium of ethylenediamine or ammonia solution was replaced with typical polar solvents, such as *N*-methyl formamide (NMF) or dimethyl sulfoxide (DMSO), to ensure the photoreactivity of the PAGs. Solvent exchange was confirmed by UV-Vis absorption analysis, which showed the disappearance of the characteristic peak at 520 nm after complete purification (Supplementary Fig. 1)<sup>40</sup>. We used a typical nonionic triazine-based PAG, 2-[2-(5-methyl furan-2-yl) vinyl]-4,6-bis(trichloromethyl)-1,3,5-triazine (MFVT), and a sulfonate-based PAG, *N*-(trifluoromethylsulfonyloxy)-1,8-naphthalimide (IM-NIT), to prepare the inks. MFVT and IM-NIT have a wide absorption spectrum range of approximately 350–400 nm and, thus, are suitable for h-line (405 nm) or i-line (365 nm) light sources (Supplementary Fig. 2). The mixed inks maintained their colloidal stability for over 14 d under dark conditions (Supplementary Fig. 3). The UV-Vis spectra of the inks showed the peaks of both ChaMs and MFVT, which indicates that these components do not react without UV irradiation (Supplementary Fig. 4). Upon UV irradiation, MFVT decomposed to produce Cl–C• and Cl• radicals, which reacted with the alcoholic solvent and released protons (H<sup>+</sup>) in the ink medium<sup>41, 42</sup>. In the case of IM-NIT, heterolytic cleavage, rather than homolytic cleavage, of the N–O bond occurred owing to the presence of the triflate anion, which is a good leaving group. The ionic intermediates produced by this process generated a photoacid (Supplementary Fig. 5)<sup>43, 44</sup>. Because chalcogens with the form M<sub>x</sub>Ch<sub>y</sub><sup>n-</sup> (Ch = S, Se) in the ChaMs have relatively high proton affinity (S: 1443–1453 kJ/mol, Se: 1408–1420 kJ/mol), the protons generated by the photoreaction of the PAGs rapidly react with the ChaM anions, causing precipitation of the ChaMs (Fig. 1b). The  $\xi$ -potential of the MoS<sub>2</sub>-based inks decreased from –28.7 to –13.6 mV upon UV irradiation (Fig. 1c), which suggested that the ChaMs lost their charges following their reaction with protons. Moreover, the solute sizes measured by dynamic light scattering (DLS) significantly increased from 106 to 295 nm upon UV irradiation (Fig. 1d), thereby demonstrating the photoreaction-induced precipitation of the ChaMs (Fig. 1e).

## Optical Printing Of Metal Chalcogenides

Based on the photoreaction of the formulated ChaM-based inks, we applied the DLP method using our inks to achieve the optical patterning of metal chalcogenides. The digital masks designed for DLP printing in this study are shown in Supplementary Fig. 6. The scanning electron microscopy (SEM) images in Figs. 2a and b show that the widths of the printed line patterns of the PtS<sub>2</sub>-based ChaMs range from 25 to 100  $\mu$ m; moreover, the minimum width observed is close to the equipment limit of 10  $\mu$ m. Various printed patterns of circles, squares, and triangles ranging in size from tens to hundreds of micrometres were also obtained. All patterned structures exhibited excellent shape fidelity and uniformity. We fabricated a large square pattern with dimensions of 1.2 cm  $\times$  1.2 cm. The root-mean-square surface

roughness of the entire printed structure was as low as 4.66 nm, which demonstrated the excellent uniformity of the proposed printing process over a centimetre-scale area (Supplementary Fig. 7). Another important advantage of our optical printing process is the high-throughput fabrication of multiple patterns on a single substrate. We successfully realised the printing of hundreds of 100  $\mu\text{m}$ -wide square arrays on a substrate in several millimetres area (Fig. 2c). These examples of high-quality 2D patterns confirm that our cost-effective and simple patterning method for 2D films may be an alternative approach to traditional lithographic techniques. As the minimum linewidths and maximum sizes of the DLP-printed patterns critically depend on the equipment specifications, we speculate that higher-resolution and larger-scale equipment could create finer and larger-scale patterns with our inks.

The direct printability of the ChaM-based inks allows for the printing of complex 2D patterns with multiple materials and 3D architectures via layer-by-layer curing. As shown in the SEM image in Fig. 2d, a geometric pattern of the  $\text{MoS}_2$ -based ChaM with a linewidth of 50  $\mu\text{m}$  was created using the DLP method. Interferometric scattering-based 3D scanning analysis of the geometric pattern obtained revealed a thickness of 45 nm with high lateral fidelity (Supplementary Fig. 8). Multiple material patterns were also successfully created on a single substrate. For example, a maze and its solution line were patterned using different ChaMs via the sequential DLP printing of  $\text{MoS}_2$ - and  $\text{PtS}_2$ -based ChaM inks. Specifically, we first patterned a  $\text{MoS}_2$ -based ChaM maze with a linewidth of 85  $\mu\text{m}$  and then patterned the solution line with a thinner linewidth of 55  $\mu\text{m}$  over this maze using  $\text{PtS}_2$ -based ChaM ink (Fig. 2e). Especially, we achieved the 3D printing of ChaMs in our system by layer-by-layer sequential deposition of  $\sim 50$  nm-thick layers on the substrate. Multiple 3D architectures composed of triangular layers printed over circular layers with a thickness of 500 nm were printed on a single substrate. The SEM and 3D scanning images in Fig. 2f show the excellent shape uniformity and fidelity of all architectures obtained. The 3D scan height profile in Fig. 2g also revealed the lateral shape fidelity of the printed architectures, which suggests minimal distortion of the pre-printed layers during the subsequent deposition process. These results clearly demonstrate the 3D printability of inorganic metal chalcogenides using our process.

## Material Characterisations Of The Printed Metal Chalcogenides

Given to the universal applicability of the photocuring mechanism, we printed a variety of ChaMs using our DLP method. The thermal decomposition characteristics of the ChaMs, crystalline metal chalcogenides, such as the functional compound semiconductors of  $\text{Sb}_2\text{S}_3$ ,  $\text{Sb}_2\text{Se}_3$ ,  $\text{Cu}_2\text{S}$ ,  $\text{SnS}$ , and  $\text{SnSe}$ , and 2D transition-metal dichalcogenides, including  $\text{SnSe}_2$ ,  $\text{MoS}_2$ , and  $\text{PtS}_2$ , were obtained by subjecting the patterned ChaMs to post-heating treatment under an inert atmosphere at temperatures of 473–620 K<sup>45</sup>. The characters of the chemical formulas corresponding to the studied materials were printed, as shown in the insets of Figs. 3a–f. Optical microscopy (OM) analysis revealed the absence of undesirable microstructural evolution in the printed structures during heat treatment (Supplementary Fig. 9). Moreover, the composition of the metal chalcogenides could be modulated by controlling the conditions of the heat treatment. Specifically, varying the temperature or holding time allowed us to

control the degree of evaporation of the chalcogen and, thus, its content in the final product. For example, heat treatment of the same sample at 573 and 673 K produced the SnSe<sub>2</sub> and SnSe phases, respectively.

The high-magnification SEM images of all samples revealed smooth and dense microstructures without the substantial formation of voids and pores (Figs. 3a–h). In particular, the printed SnSe, SnSe<sub>2</sub>, and SnS films showed a 2D plate-like morphology, which can be attributed to the active lateral 2D growth of the grains, which are well known to have 2D layered structures. This unique microstructure was supported by the X-ray diffraction (XRD) patterns of the samples, which showed peaks corresponding to specific axes. For example, the XRD patterns of SnSe and SnSe<sub>2</sub> (Figs. 3c and d) showed the *c*- and *a*-axis peaks of the (200), (400), and (800) planes, indicating strong texturing in the microstructures of these samples. In addition, the XRD patterns of the other samples exhibited peaks corresponding to those of the bulk references, which indicates their high crystallinity. The 2D transition-metal dichalcogenides MoS<sub>2</sub> and PtS<sub>2</sub> were characterised by Raman spectroscopy. The Raman spectrum of the printed MoS<sub>2</sub> layer showed peaks at ~ 380 and ~ 403 cm<sup>-1</sup>, which correspond to the E<sub>2g</sub> and A<sub>1g</sub> vibration modes of 2H-MoS<sub>2</sub> (Fig. 3g)<sup>46</sup>. The two intense peaks at approximately ~ 300 and ~ 339 cm<sup>-1</sup> in the Raman spectrum of the PtS<sub>2</sub> thin film were well matched to the E<sub>1g</sub> and A<sub>1g</sub> modes, respectively, of the PtS<sub>2</sub> reference phase (Fig. 3h)<sup>47</sup>. These results demonstrate the high crystallinity and controllable micro-scale crystallographic textures of the patterned metal dichalcogenides obtained via our process.

## Functional Properties Of The Printed Metal Chalcogenides

The functionality of the patterned metal chalcogenide semiconductors was demonstrated in terms of their electrical properties, which were obtained using Hall measurements; the charge carrier mobility and concentration of these materials were then obtained. We selected Cu<sub>2</sub>S and SnSe<sub>2</sub> as model p-type and n-type semiconductors, respectively, because they are known to be low-cost semiconductors exhibiting good electrical properties<sup>48, 49</sup>. Here, we fabricated 2D Cu<sub>2</sub>S and SnSe<sub>2</sub> samples using the DLP method and then annealed them at 732 and 573 K for 5, 10, 15, and 7, 10, or 15 min. The annealing temperatures were selected after considering the thermal stability of the materials to conserve their stoichiometric composition and microstructural integrity. The Hall measurements of the printed Cu<sub>2</sub>S clearly indicated p-type characteristics. As the annealing time increased from 5 to 15 min, the room-temperature hole concentration of the samples decreased from  $1.58 \times 10^{20}$  to  $6.29 \times 10^{19}$  cm<sup>-3</sup> (Fig. 4a), which agrees with the reported hole concentration range of bulk Cu<sub>2</sub>S<sup>50</sup>. Because the intrinsic defects of Cu vacancies in Cu<sub>2</sub>S act as hole donors, longer annealing times could promote the evaporation of S, eventually decreasing the number of Cu vacancy defects. The hole mobility of the samples also increased from 1.29 to 3.89 cm<sup>2</sup> V<sup>-1</sup> s<sup>-1</sup> with increasing annealing time (Fig. 4a), likely because longer annealing times could decrease the number of Cu vacancy point defects and lead to higher crystallinity. These findings were supported by the SEM images of the samples (Supplementary Fig. 10), which showed fewer pinholes and cracks in the microstructures of samples heated for longer durations. By comparison, the SnSe<sub>2</sub> samples showed n-type characteristics, and their electron concentration, at  $\sim 1.0 \times 10^{19}$  cm<sup>-3</sup>, remained nearly

constant regardless of the annealing time (Fig. 4b). Furthermore, the electron mobility of the samples increased from 1.06 to 2.25 cm<sup>2</sup> V<sup>-1</sup> s<sup>-1</sup> as the annealing time increased (Fig. 4b), which suggests grain growth, as supported by their SEM images (Supplementary Fig. 11). In general, the maximum electron mobilities of the printed n- and p-type samples exceeded 1 cm<sup>2</sup> V<sup>-1</sup> s<sup>-1</sup> under optimal conditions. Such values are comparable with those reported for metal chalcogenide and inorganic patterns fabricated by traditional lithographic techniques or other printing methods, as summarised in Supplementary Table 1.

Given the excellent electrical properties of the Cu<sub>2</sub>S and SnSe<sub>2</sub> samples, they may be applied to energy devices, such as thermoelectric devices. These devices are of tremendous interest because they can achieve direct heat–electricity conversion, which is useful in various technological applications, such as energy harvesting, local thermal management, and thermal sensors<sup>51–54</sup>. The electronic devices that have emerged in recent years require autonomous energy systems, which, in turn, demand system-adaptable energy sources integrated into them<sup>55</sup>. In this context, patterned micro thermoelectric generators may be ideal candidates as auxiliary power sources for these systems. The materials used in these devices must have high microstructural quality and tight engineering to preserve their thermoelectric properties and optimise their trade-off properties. Such materials would provide an excellent model system for demonstrating the feasibility of our process. Thus, we characterised the temperature-dependent thermoelectric properties of the Cu<sub>2</sub>S and SnSe<sub>2</sub> samples. The temperature-dependent electrical conductivity and Seebeck coefficients of the printed Cu<sub>2</sub>S samples were measured from room temperature to 600 K (Figs. 4c and e). As expected, the Cu<sub>2</sub>S samples exhibited p-type semiconductor behaviour, as indicated by their positive Seebeck coefficients. Moreover, fluctuations in both electrical conductivity and Seebeck coefficient were clearly observed in the temperature range of 350–500 K, in agreement with the typical behaviour of Cu<sub>2-x</sub>S crystals, which exhibit a phase transition from the low chalcocite phase to the high chalcocite phase in the corresponding temperature range<sup>49, 50</sup>. This phase transition reflects the good crystallinity of our Cu<sub>2</sub>S samples fabricated by DLP printing. Among the samples investigated, that annealed for 15 min showed the highest room-temperature electrical conductivity (1,000 S m<sup>-1</sup>) owing to its high carrier mobility and concentration (Fig. 4c). This value corresponds to approximately 20% of the electrical conductivity previously reported for Cu<sub>2</sub>S bulk samples prepared by spark plasma sintering<sup>50</sup>. The Seebeck coefficients of all samples showed a positive dependence on temperature owing to their high carrier concentration. The sample annealed for 10 min showed a maximum Seebeck coefficient of 230 μV K<sup>-1</sup> at 600 K (Fig. 4e), which is comparable with the reported value for Cu<sub>2</sub>S bulk materials<sup>50</sup>. The sample annealed for 15 min also showed the highest power factor (0.187 μW cm<sup>-1</sup> K<sup>-2</sup>) at 600 K (Fig. 4g).

The temperature-dependent electrical conductivity and Seebeck coefficients of the printed SnSe<sub>2</sub> samples were also measured in the temperature range of 300–550 K (Figs. 4d and f). The electrical conductivity of all samples increased with increasing temperature. Among the samples investigated, that annealed for 15 min showed the highest electrical conductivity of 272 S m<sup>-1</sup> at room temperature (Fig. 4d). This value is approximately 30% of the electrical conductivity reported for undoped high-quality SnSe<sub>2</sub> single-crystal

bulk samples grown by the temperature gradient method, which indicates the high quality of our samples fabricated by the DLP method<sup>56</sup>. The Seebeck coefficients of the samples ranged from  $-287$  to  $-192 \mu\text{V K}^{-1}$  (Fig. 4f), which are slightly lower than those observed in  $\text{SnSe}_2$  single-crystals; such values may be attributed to the high carrier concentration of the samples<sup>56</sup>. The maximum power factor of the samples at 550 K was approximately  $0.31 \mu\text{W cm}^{-1} \text{K}^{-2}$  (Fig. 4h). These results demonstrate the feasibility of our method for patterning highly functional crystalline metal chalcogenides without substantial losses in their intrinsic properties.

## Fabrication And Evaluation Of Micro Thermoelectric Generator

We fabricated a micro-scale thermoelectric generator via the DLP printing of multiple p-type  $\text{Cu}_2\text{S}$  and n-type  $\text{SnSe}_2$  legs. DLP-based printing enables the simultaneous, rapid, and straightforward fabrication of several tens of thermoelectric legs of identical printing quality. We designed the shapes of the p-type and n-type legs to enable their direct connection without the need for metal electrodes, which is beneficial for simplifying the manufacture of the devices. Using a digital mask composed of 10 pairs of  $300 \mu\text{m}$ -wide p-type and n-type legs (Supplementary Figs. 6g and h), we fabricated the desired patterns via a sequential patterning method. Here, the p-type  $\text{Cu}_2\text{S}$  legs were patterned and heat-treated at 723 K, and the n-type  $\text{SnSe}_2$  legs were patterned and annealed at 573 K (Fig. 5a). The power performance of the printed micro-scale thermoelectric generator was measured as each side was heated and cooled using a ceramic heater and Peltier cooler, respectively (Supplementary Fig. 12). During heating, the hot-side temperature gradually increased to 370 K, while the cold-side temperature remained at approximately 304 K (Supplementary Fig. 13). As the measured temperatures increased, the output voltage and power increased linearly and quadratically, respectively, demonstrating reliable power generation (Fig. 5b). At a maximum temperature difference of 65 K, the maximum output voltage and power density of the micro-scale thermoelectric generator reached 223.5 mV and  $0.564 \text{ mW cm}^{-2}$ , respectively (Fig. 5c). Such power generation performance clearly demonstrates the practicability of our DLP-based optical printing process for fabricating integratable micro-scale 2D or 3D devices with diverse heterostructured functional materials. Indeed, our process may ultimately be able to facilitate the integration of electronic devices into other systems.

## Discussion

In summary, we established a generalised DLP-based optical printing technology to obtain diverse crystalline metal chalcogenides with 2D and 3D architectures by developing photocurable ChaM-based inorganic inks. The combination of mask-less DLP-based printing and our photocurable inorganic inks led to the facile fabrication of various inorganic materials with 2D and 3D architectures and excellent shape uniformity and fidelity. Our method features universal printability, including diverse functional metal chalcogenides and 2D layered transition-metal dichalcogenides. We demonstrated the feasibility of our approach by fabricating and evaluating a micro-scale thermoelectric device. Unlike previous optical printing processes, our approach provides a single-step patterning method that enables the direct use of

inks, which could significantly reduce the manufacturing cost and time, and raises the possibility of building 3D architectures. The proposed process expands the availability of optically printable materials to inorganic semiconductors, which were previously limited, photocurable polymers, and composites with inorganic fillers. We believe that our technology, in combination with high-resolution equipment, such as two-photon lithography, can realise the patterning of inorganic materials with excellent quality and resolution. Our DLP-based optical printing technology presents an alternative approach to photolithography and can serve as a platform technology for the cost-effective, simple, and high-resolution direct architecturing of inorganic materials.

## Methods

### Materials

Antimony(III) sulfide (99.995%, Sigma Aldrich), antimony(III) selenide (99.99%, Sigma Aldrich), tin powder (99.8%, 325 mesh, Acros Organics), selenium powder (99.999%, 200 mesh, Alfa Aesar), sulfur (99.998%, Sigma Aldrich), copper powder (99%, Alfa Aesar), ammonium sulfide solution (40–48 wt% in H<sub>2</sub>O, Sigma Aldrich), chloroplatinic acid solution (8 wt% in H<sub>2</sub>O, Sigma Aldrich), ammonium tetrathiomolybdate (99.97%, Sigma Aldrich), 2-[2-(5-methylfuran-2-yl)vinyl]-4,6-bis(trichloromethyl)-1,3,5-triazine (MFVT, TCI), *N*-(trifluoromethylsulfonyloxy)-1,8-naphthalimide (IM-NIT, WIMAS Corp.), ethylenediamine ( $\geq$  99.5%, Sigma Aldrich), 1,2-ethanedithiol ( $\geq$  98.0%, Sigma Aldrich), anhydrous acetonitrile (99.8%, Sigma Aldrich), anhydrous toluene (99.8%, Sigma Aldrich), *N*-methyl formamide (99%, Sigma Aldrich), anhydrous dimethyl sulfoxide ( $\geq$  99.9%, Sigma Aldrich), ethyl alcohol (99.5%, Samchun), and methyl alcohol (99.5%, Samchun) were used in the experiments. All chemicals and reagents were used as received without further purification.

### Material Characterisation

Scanning electron microscopy (SEM): The shapes and microstructures of the various printed metal chalcogenides were obtained using a field-emission scanning electron microscope (FE-SEM Nano230) operated at 10 kV. Elemental analysis of the printed metal chalcogenides was performed by energy-dispersive X-ray spectroscopy (EDS) using the same SEM instrument.

High-power X-ray diffractometry (XRD): The XRD patterns of the printed metal chalcogenides were acquired using a D/MAX2500V/PC instrument (Rigaku) with a Cu-rotating anode X-ray source operated at 40 kV and 200 mA.

UV-vis absorption spectroscopy: The UV-absorption spectra of the photocurable ChaM-based inks and PAG solution were measured using a UV-vis spectrophotometer (UV-2600, Shimadzu) at room temperature.

Confocal Raman spectroscopy: The Raman spectra of the printed MoS<sub>2</sub> and PtS<sub>2</sub> layers were obtained using a confocal Raman microscope (Alpha300R, WITec) at room temperature with an excitation wavelength of 532 nm.

Interferometric scattering-based 3D measurements: The 3D scanned images, height profile, and roughness of the printed structures were obtained by an NV-3000 instrument (NanoSystem) using interferometric scattering.

$\zeta$ -potential and dynamic light scattering (DLS): The  $\zeta$ -potential and DLS sizes of the photocurable ChaM-based inks were measured before and after UV irradiation using a Zetasizer Nano-ZS (Malvern).

Optical microscopy (OM): OM images of the printed layers were obtained using a semi-motorised fluorescence microscope BX53M (Olympus).

## Synthesis of the chalcogenidometallate solutions

*Sb-based chalcogenidometallates.* Sb-based ChaM solutions were synthesised using an amine/thiol alkali solvent with additional purification. The overall synthetic process was performed in a N<sub>2</sub>-filled glove box. In a typical experiment, 33.97 mg of Sb<sub>2</sub>S<sub>3</sub> powder was added to a mixture of 1 ml of ethylenediamine and 0.1 ml of ethanedithiol (10:1, v/v) in a 10 ml vial with a stirring bar. The Sb<sub>2</sub>S<sub>3</sub> powders were dissolved on a 50°C hot plate in a glove box for 2.5 h with stirring until the powders were completely dissolved. Thereafter, the anti-solvent acetonitrile (22 ml) was added to the Sb<sub>2</sub>S<sub>3</sub> solution for purification (20:1, v/v). This mixture was centrifuged at 7,800 rpm for 5 min to precipitate the purified ChaM precursors. The precipitate was redispersed in 1 ml of DMSO, added with 5 ml of acetonitrile (5:1, v/v), and centrifuged at 10,000 rpm for 5 min. Finally, the precipitate was dispersed in 0.5 ml of DMSO. Exactly 56.15 mg of Sb<sub>2</sub>Se<sub>3</sub> powder was added to a mixture of ethylenediamine and ethanedithiol as described above. The Sb<sub>2</sub>Se<sub>3</sub> powder was then dissolved for 1 h. Purification via the same method described above followed. Finally, the precipitate was redispersed in 1 ml of DMSO.

*Sn-based chalcogenidometallates.* To obtain SnS, we added Sn (110 mg) and S (30 mg) powders to a mixture of 1.6 ml of ethylenediamine and 0.16 ml of ethanedithiol (10:1, v/v) in a 10 ml vial with a stirring bar. The Sn and S powders were stirred for 12 h until the powders were completely dissolved and the solution became colourless. The anti-solvent acetonitrile was subsequently added to the SnS solution for purification (20:1, v/v), and the mixture was centrifuged at 7,800 rpm for 5 min. The precipitate was redispersed in NMF, added with anhydrous toluene (3:1, v/v), and centrifuged at 10,000 rpm for 5 min for purification. Finally, the precipitate was dispersed in 1 ml of NMF. To obtain SnSe, we added 90 mg of Sn powder and 60 mg of Se powder to a mixture of 1.6 ml of ethylenediamine and 0.16 ml of ethanedithiol (10:1, v/v) in a 10 ml vial. The mixture was then dissolved for 1 h and 40 min. Purification via the same method employed for SnS followed. Finally, the precipitate was redispersed in 2 ml of NMF.

*Cu-based chalcogenidometallates.* Cu<sub>2</sub>Se powder was synthesised by the high-energy ball-milling of Cu and Se powders as described in a previous report<sup>23</sup>. Ball-milled Cu<sub>2</sub>Se powder (103 mg) was added to a mixture of 1 ml of ethylenediamine and 0.1 ml of ethanedithiol (10:1, v/v) in a 10 ml vial with a stirring bar. The Cu<sub>2</sub>Se powders were mixed for 45 min until they were completely dissolved. The anti-solvent acetonitrile (5.5 ml) was added to the Cu<sub>2</sub>Se solutions (5:1, v/v) to purify the synthesised ChaM. This

mixture was centrifuged at 7,800 rpm for 5 min to precipitate the purified ChaM precursors, which were then redispersed in 1 ml of DMSO. This purification step was repeated twice.

*Ammonium thioplatinate.* Ammonium thioplatinate was synthesised using a modified method based on a previous report<sup>37</sup>. Exactly 3 g of S powder was added to 10 ml of an ammonium sulfide/distilled water solution (5 ml each). The mixture was stirred at room temperature until its colour turned red, signifying the formation of ammonium polysulfides. Then, 1.25 ml of chloroplatinic acid solution was slowly dropped into this red solution. The solution was stirred overnight and changed in colour from black-red to orange. The precipitate was then centrifuged at 7,000 rpm for 3 min. The precipitates were purified thrice with methanol and toluene (1:14, v/v) by centrifugation. Ammonium thioplatinate was redispersed in NMF at a concentration of 10 mg/ml.

*Ammonium tetrathiomolybdate.* Ammonium tetrathiomolybdate ((NH<sub>4</sub>)<sub>2</sub>MoS<sub>4</sub>) (90 mg) was dissolved in 2 ml of NMF (2 ml; 45 mg/ml).

The completely dissolved inorganic solutions maintained their solubility for several months without any precipitation.

### **DLP-based optical printing process**

*Photocurable inorganic inks.* 2-[2-(5-Methylfuran-2-yl)vinyl]-4,6-bis(trichloromethyl)-1,3,5-triazine (MFVT) and *N*-(trifluoromethylsulfonyloxy)-1,8-naphthalimide (IM-NIT) were dissolved in several organic solvents, including ethanol, acetonitrile, and DMSO. The solubility limits of PAG differed for each solvent. In our experiments, we used 0.02 M PAG-acetonitrile and 0.02 M) PAG-DMSO. Photocurable inorganic inks of the metal chalcogenides were prepared using a combination of ChaM-based inks and PAG solutions. The most important aspect of the DLP-based printing process is that the solubility of the ChaM-based inks–PAG mixture must be well maintained without any precipitation prior to UV exposure. Therefore, optimisation of the ChaM-based ink/PAG ratio is a key element for DLP-based printing. After a careful analysis of the detailed reactions of each photocurable inorganic ink, Sb<sub>2</sub>S<sub>3</sub> (DMSO)/PAG-MFVT (0.02 M, DMSO) (1:3 v/v), Sb<sub>2</sub>Se<sub>3</sub> (DMSO)/PAG-IM-NIT (0.02 M, DMSO) (1:1 v/v), SnS (NMF)/PAG-IM-NIT (0.02 M, ACN) (1:1.5 v/v), SnSe (NMF)/PAG-IM-NIT (0.02 M, DMSO) (1:1.25 v/v), Cu<sub>2</sub>S (DMSO)/PAG-MFVT (0.02 M, DMSO) (1:3 v/v), MoS<sub>2</sub> (NMF)/PAG-MFVT (0.02 M, ACN) (1:2.5 v/v), PtS<sub>2</sub> (NMF)/PAG-MFVT (0.02 M, ACN) (1:1.25 v/v) were finally prepared. These conditions can be changed according to various ink parameters, such as the ChaM solution concentration, PAG concentration, type, and solvent.

*DLP-based optical printing.* Two DLP systems were used for DLP-based optical printing. The first system uses a commercial DLP 3D printer (Nobel Superfine, XYZ Printing), which can provide 405 nm UV LED illumination over an area of 64 mm × 120 mm with a minimum X-Y resolution of 50 μm. This printer could produce sliced stl image files using XYZware Novel software. Because this commercial DLP 3D printing system is installed in a UV-protected N<sub>2</sub>-filled glovebox, air-sensitive photocurable inorganic inks can be printed on this system. The second system uses hand-crafted DLP equipment (Luxbeam Rapid

System, Visiotech). This system can illuminate a maximum area of 5 mm × 3 mm with 365 nm UV light. The maximum power and minimum resolution were 4 W and approximately 10 μm, respectively. The automation program for optical printing uses g-code-based Visual Studio with sliced 3D images. The 3D architectures were obtained via a Z-stage (Linax, Lxc), which is capable of controlled 100 nm-scale movement, and the light exposure was adjusted by a shutter (Uniblitz, VED24).

### **Heat treatment of the printed metal chalcogenides**

Antimony sulfide ( $\text{Sb}_2\text{S}_3$ ) was annealed at 573 K for 1 min in ambient sulfur. Antimony selenide ( $\text{Sb}_2\text{Se}_3$ ) was obtained by heat treatment at 573 K for 1 min. Tin sulfide ( $\text{SnS}$ ) was recrystallised at 623 K for 1 min. Tin diselenide ( $\text{SnSe}_2$ ) was annealed at 573 K for 10 min, and tin selenide ( $\text{SnSe}$ ) was annealed at 723 K for 3 min. Copper sulfide ( $\text{Cu}_2\text{S}$ ) was obtained by heat treatment at 723 K for 10 min. The heat treatment of the ChaM-based printed layers was conducted in a  $\text{N}_2$ -filled glovebox. Molybdenum disulfide ( $\text{MoS}_2$ ) was obtained via a two-step heat treatment. After 5 min of annealing at 573 K in ambient sulfur, a stable  $\text{MoS}_3$  phase was formed. Additional annealing at 723 K in 15%  $\text{H}_2$  was subsequently conducted in a tube furnace for 10 min. Platinum disulfide ( $\text{PtS}_2$ ) was subjected to a two-step heat treatment. The pre-heating treatment was conducted at 873 K for 1 h in a tube furnace under a  $\text{N}_2$  atmosphere. The printed layers were annealed at 773 K for 30 min in ambient sulfur in a  $\text{N}_2$ -filled glove box.

### **Thermoelectric properties of the printed layers**

The Hall effect was measured at room temperature using a Hall measurement system (HMS-5000, ECOPIA). The charge carrier mobilities of the printed  $\text{Cu}_2\text{S}$  and  $\text{SnSe}_2$  were calculated using the obtained Hall coefficients and electrical conductivities measured by the Van der Pauw method. The temperature-dependent electrical conductivity and Seebeck coefficients of the printed  $\text{Cu}_2\text{S}$  and  $\text{SnSe}_2$  were measured using thermal analysis equipment (SBA 458 Nemesis, Netzsch) under inert conditions in the temperature range of 300–600 K. The typical size of a test specimen was 1.2 cm × 1.2 cm.

### **Fabrication and evaluation of a micro-scale thermoelectric generator**

Approximately 600 μL of photocurable  $\text{Cu}_2\text{S}$ -based ink was poured on a glass substrate in a ink bath to print p-type thermoelectric legs. A digital mask with 300 μm-scale thermoelectric legs was exposed to UV light from the DLP 3D printer. The printed p-type  $\text{Cu}_2\text{S}$  legs were rinsed with the same polar solvent and annealed at 723 K for 15 min on a hot plate in a  $\text{N}_2$ -filled glovebox. Approximately 600 μL of photocurable  $\text{SnSe}$ -based ink was poured onto a p-type leg-patterned glass substrate to obtain n-type thermoelectric legs. The same procedures were performed using a modified n-type thermoelectric leg digital mask. The printed n-type  $\text{SnSe}_2$  legs were rinsed and annealed at 573 K for 15 min. Ten pairs of p- and n-type thermoelectric legs were securely connected. To measure the power generation of the fabricated micro-scale thermoelectric generator, we connected two K-type thermocouples to a Keithley 2000 multimeter and the edges of the thermoelectric legs on the hot (i.e. on the ceramic heater) and cold (i.e. on the Peltier cooler) sides of the generator. The cold-side temperature was maintained at

approximately 304 K, whereas the hot-side temperature was gradually increased to 370 K. The micro thermoelectric generator was connected to a Keithley 2400 instrument, and the output voltages were measured for five temperature-difference cases with an applied sweep current. The output power  $P$  was calculated using the formula  $P = V \times I$ , where  $V$  is the voltage and  $I$  is the current.

## Declarations

### Data availability

The data that support the plots within this paper and other findings of this study are available from the corresponding author upon reasonable request.

### Acknowledgements

This work was supported by the National Research Foundation of Korea (NRF) grant funded by the Korea government (the Ministry of Science and ICT) (NRF-2018M3A7B8060697, NRF-2022R1A2C3009129, and NRF-2020M3D1A1110502), and the UNIST Research Fund (1.220024.01).

### Author Contributions

S.B., H.W.B., and S.J. contributed equally to this work. S.B., H.W.B., S.J., J.L., and J.S.S. designed the experiments, analysed the data, and wrote the paper. S.B., H.W.B., D.H.G., W.C., Y.E.P and S.C. carried out the synthesis and basic characterization of materials. S.B., H.W.B. and S.J. performed the printing of metal chalcogenides. S.H.H. performed the characterization of thermoelectric properties. All authors discussed the results and commented on the manuscript.

### Competing interests

The authors declare no competing interests.

## References

1. Xia, Y., Rogers, J. A., Paul, K. E. & Whitesides, G. M. Unconventional Methods for Fabricating and Patterning Nanostructures. *Chem. Rev.* **99**, 1823–1848 (1999).
2. Liddle, J. A. & Gallatin, G. M. Nanomanufacturing: A Perspective. *ACS Nano* **10**, 2995–3014 (2016).
3. Wang, K., Xing, G., Song, Q. & Xiao, S. Micro- and Nanostructured Lead Halide Perovskites: From Materials to Integrations and Devices. *Adv. Mater.* **33**, e2000306 (2021).
4. Briseno, A. L. *et al.* Patterning organic single-crystal transistor arrays. *Nature* **444**, 913–917 (2006).
5. Aizenberg, J., Muller, D. A., Grazul, J. L. & Hamann, D. R. Direct fabrication of large micropatterned single crystals. *Science* **299**, 1205–1208 (2003).

6. Wang, B. *et al.* Foundry-compatible high-resolution patterning of vertically phase-separated semiconducting films for ultraflexible organic electronics. *Nat. Commun.* **12**, 4937 (2021).
7. Chou, S. Y., Krauss, P. R. & Renstrom, P. J. Imprint Lithography with 25-Nanometer Resolution. *Science* **272**, 85–87 (1996).
8. Perl, A., Reinhoudt, D. N. & Huskens, J. Microcontact Printing: Limitations and Achievements. *Adv. Mater.* **21**, 2257–2268 (2009).
9. Tu, M. *et al.* Direct X-ray and electron-beam lithography of halogenated zeolitic imidazolate frameworks. *Nat. Mater.* **20**, 93–99 (2021).
10. Legrand, A. *et al.* Spatiotemporal Control of Supramolecular Polymerization and Gelation of Metal-Organic Polyhedra. *J. Am. Chem. Soc.* **143**, 3562–3570 (2021).
11. Chen, Y. *et al.* A universal method for depositing patterned materials in situ. *Nat. Commun.* **11**, 5334 (2020).
12. Ito, T. & Okazaki, S. Pushing the limits of lithography. *Nature* **406**, 1027–1031 (2000).
13. Ligon, S. C., Liska, R., Stampfl, J., Gurr, M. & Mulhaupt, R. Polymers for 3D Printing and Customized Additive Manufacturing. *Chem. Rev.* **117**, 10212–10290 (2017).
14. Zhao, Z., Tian, X. & Song, X. Engineering materials with light: recent progress in digital light processing based 3D printing. *J. Mater. Chem. C* **8**, 13896–13917 (2020).
15. Fantino, E. *et al.* 3D Printing of Conductive Complex Structures with In Situ Generation of Silver Nanoparticles. *Adv. Mater.* **28**, 3712–3717 (2016).
16. Mu, Q. *et al.* Digital light processing 3D printing of conductive complex structures. *Addit. Manuf.* **18**, 74–83 (2017).
17. Kim, K. *et al.* 3D optical printing of piezoelectric nanoparticle-polymer composite materials. *ACS Nano* **8**, 9799–9806 (2014).
18. He, M., Zhao, Y., Wang, B., Xi, Q., Zhou, J. & Liang, Z. 3D Printing Fabrication of Amorphous Thermoelectric Materials with Ultralow Thermal Conductivity. *Small* **11**, 5889–5894 (2015).
19. Zhang, R. *et al.* Metal-metal chalcogenide molecular precursors to binary, ternary, and quaternary metal chalcogenide thin films for electronic devices. *Chem. Commun.* **52**, 5007–5010 (2016).
20. Talapin, D. V., Lee, J. S., Kovalenko, M. V. & Shevchenko, E. V. Prospects of colloidal nanocrystals for electronic and optoelectronic applications. *Chem. Rev.* **110**, 389–458 (2010).

21. Lin, Z. *et al.* A Solution Processable High-Performance Thermoelectric Copper Selenide Thin Film. *Adv. Mater.* **29**, 1606662 (2017).
22. Burton, M. R. *et al.* Thin Film Tin Selenide (SnSe) Thermoelectric Generators Exhibiting Ultralow Thermal Conductivity. *Adv. Mater.* **30**, e1801357 (2018).
23. Choo, S. *et al.* Cu<sub>2</sub>Se-based thermoelectric cellular architectures for efficient and durable power generation. *Nat. Commun.* **12**, 3550 (2021).
24. Zheng, W. *et al.* Patterning two-dimensional chalcogenide crystals of Bi<sub>2</sub>Se<sub>3</sub> and In<sub>2</sub>Se<sub>3</sub> and efficient photodetectors. *Nat. Commun.* **6**, 6972 (2015).
25. Wang, Y., Fedin, I., Zhang, H. & Talapin, D. V. Direct optical lithography of functional inorganic nanomaterials. *Science* **357**, 385–388 (2017).
26. Yang, J. *et al.* High-resolution patterning of colloidal quantum dots via non-destructive, light-driven ligand crosslinking. *Nat. Commun.* **11**, 2874 (2020).
27. Tang, X., Chen, M., Ackerman, M. M., Melnychuk, C. & Guyot-Sionnest, P. Direct Imprinting of Quasi-3D Nanophotonic Structures into Colloidal Quantum-Dot Devices. *Adv. Mater.* **32**, e1906590 (2020).
28. Wang, W., Pfeiffer, P. & Schmidt-Mende, L. Direct Patterning of Metal Chalcogenide Semiconductor Materials. *Adv. Funct. Mater.* **30**, 2002685 (2020).
29. Cho, H. *et al.* Direct Optical Patterning of Quantum Dot Light-Emitting Diodes via In Situ Ligand Exchange. *Adv. Mater.* **32**, e2003805 (2020).
30. Mitzi, D. B., Kosbar, L. L., Murray, C. E., Copel, M. & Afzali, A. High-mobility ultrathin semiconducting films prepared by spin coating. *Nature* **428**, 299–303 (2004).
31. Webber, D. H & Brutchey, R. L. Alkahest for V<sub>2</sub>VI<sub>3</sub> chalcogenides: dissolution of nine bulk semiconductors in a diamine-dithiol solvent mixture. *J. Am. Chem. Soc.* **135**, 15722–15725 (2013).
32. Kovalenko, M. V., Scheele, M. & Talapin, D. V. Colloidal nanocrystals with molecular metal chalcogenide surface ligands. *Science* **324**, 1417–1420 (2009).
33. Dolzhenkov, D. S. *et al.* Materials chemistry. Composition-matched molecular "solders" for semiconductors. *Science* **347**, 425–428 (2015).
34. Heo, S. H., Jo, S., Cho, S. & Son, J. S. Solution-Processed Metal Chalcogenide Thermoelectric Thin Films. In: *Thin Film and Flexible Thermoelectric Generators, Devices and Sensors* (2021).
35. McCarthy, C. L. & Brutchey, R. L. Solution processing of chalcogenide materials using thiol-amine "alkahest" solvent systems. *Chem. Commun.* **53**, 4888–4902 (2017).

36. Heo, S. H. *et al.* Composition change-driven texturing and doping in solution-processed SnSe thermoelectric thin films. *Nat. Commun.* **10**, 864 (2019).
37. Choi, W. *et al.* Thiometallate precursors for the synthesis of supported Pt and PtNi nanoparticle electrocatalysts: Size-focusing by S capping. *Nanoscale* **12**, 10498–10504 (2020).
38. Crosby, G. A. & Demas, J. N. Quantum efficiencies on transition metal complexes. II. Charge-transfer luminescence. *J. Am. Chem. Soc.* **93**, 2841–2847 (2002).
39. Ban, H. W. *et al.* Molybdenum and Tungsten Sulfide Ligands for Versatile Functionalization of All-Inorganic Nanocrystals. *J. Phys. Chem. Lett.* **7**, 3627–3635 (2016).
40. Lin, Z. *et al.* Cosolvent approach for solution-processable electronic thin films. *ACS Nano* **9**, 4398–4405 (2015).
41. Zhang, J., Xiao, P., Morlet-Savary, F., Graff, B., Fouassier, J. P. & Lalevée, J. A known photoinitiator for a novel technology: 2-(4-methoxystyryl)-4,6-bis(trichloromethyl)-1,3,5-triazine for near UV or visible LED. *Polym. Chem.* **5**, 6019–6026 (2014).
42. Pohlers, G., Scaiano, J. C., Sinta, R., Brainard, R. & Pai, D. Mechanistic Studies of Photoacid Generation from Substituted 4,6-Bis(trichloromethyl)-1,3,5-triazines. *Chem. Mater.* **9**, 1353–1361 (1997).
43. Malval, J.-P. *et al.* On the cleavage process of the N-trifluoromethylsulfonyloxy-1,8-naphthalimide photoacid generator. *Chem. Phys. Lett.* **443**, 323–327 (2007).
44. Ortica, F., Scaiano, J. C., Pohlers, G., Cameron, J. F. & Zampini, A. Laser Flash Photolysis Study of Two Aromatic N-Oxyimidosulfonate Photoacid Generators. *Chem. Mater.* **12**, 414–420 (2000).
45. Mitzi, D. B. Solution Processing of Chalcogenide Semiconductors via Dimensional Reduction. *Adv. Mater.* **21**, 3141–3158 (2009).
46. Liu, K. K. *et al.* Growth of large-area and highly crystalline MoS<sub>2</sub> thin layers on insulating substrates. *Nano Lett.* **12**, 1538–1544 (2012).
47. Liu, J. *et al.* Efficient photocatalytic hydrogen evolution mediated by defect-rich 1T-PtS<sub>2</sub> atomic layer nanosheet modified mesoporous graphitic carbon nitride. *J. Mater. Chem. A* **7**, 18906–18914 (2019).
48. Kumar, M., Rani, S., Singh, Y., Gour, K. S. & Singh, V. N. Tin-selenide as a futuristic material: properties and applications. *RSC Adv.* **11**, 6477–6503 (2021).
49. He, Y. *et al.* High thermoelectric performance in non-toxic earth-abundant copper sulfide. *Adv. Mater.* **26**, 3974–3978 (2014).

50. Yao, Y., Zhang, B.-P., Pei, J., Liu, Y.-C. & Li, J.-F. Thermoelectric performance enhancement of Cu<sub>2</sub>S by Se doping leading to a simultaneous power factor increase and thermal conductivity reduction. *J. Mater. Chem. C* **5**, 7845–7852 (2017).
51. Zaferani, S. H., Sams, M. W., Ghomashchi, R. & Chen, Z.-G. Thermoelectric coolers as thermal management systems for medical applications: Design, optimization, and advancement. *Nano Energy* **90**, 106572 (2021).
52. Vieira, E. M. F. *et al.* Enhanced thermoelectric properties of Sb<sub>2</sub>Te<sub>3</sub> and Bi<sub>2</sub>Te<sub>3</sub> films for flexible thermal sensors. *J. Alloy. Comp.* **774**, 1102–1116 (2019).
53. Zeng, M. *et al.* Printing thermoelectric inks toward next-generation energy and thermal devices. *Chem. Soc. Rev.* **51**, 485–512 (2022).
54. Choi, J. *et al.* High-Performance, Wearable Thermoelectric Generator Based on a Highly Aligned Carbon Nanotube Sheet. *ACS Appl. Energy Mater.* **3**, 1199–1206 (2019).
55. Haras, M. & Skotnicki, T. Thermoelectricity for IoT – A review. *Nano Energy* **54**, 461–476 (2018).
56. Pham, A.-T. *et al.* High-Quality SnSe<sub>2</sub> Single Crystals: Electronic and Thermoelectric Properties. *ACS Appl. Energy Mater.* **3**, 10787–10792 (2020).

## Figures

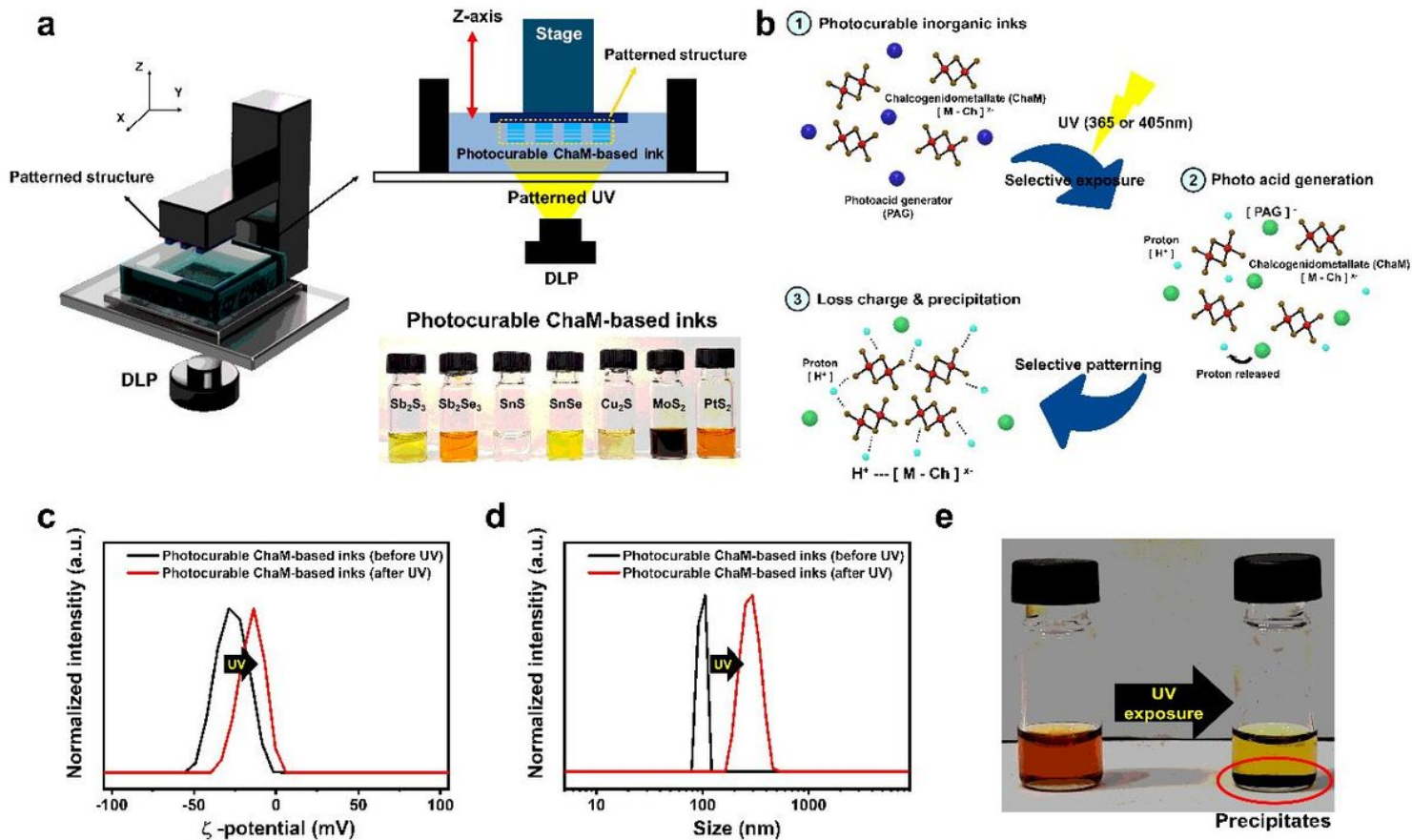


Figure 1

**Generalised optical printing of metal chalcogenide.** **a** Schematic of the DLP-based optical printing of ChaM-based inks. **b** Photocuring mechanism of the photocurable ChaM-based inks. **c**  $\zeta$ -potential, **d** DLS size, and **e** photograph of the photocurable ChaM-based inks before and after UV irradiation.

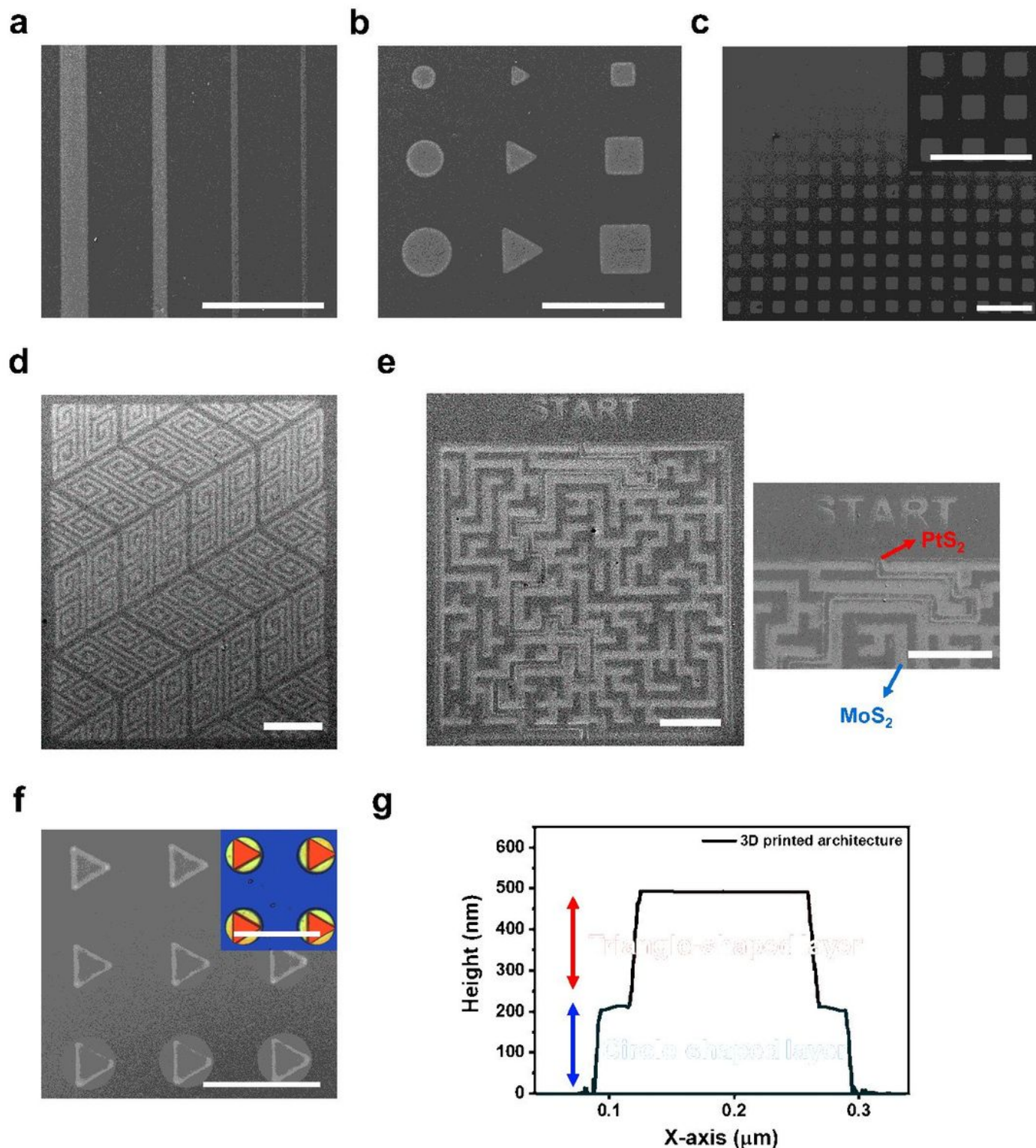
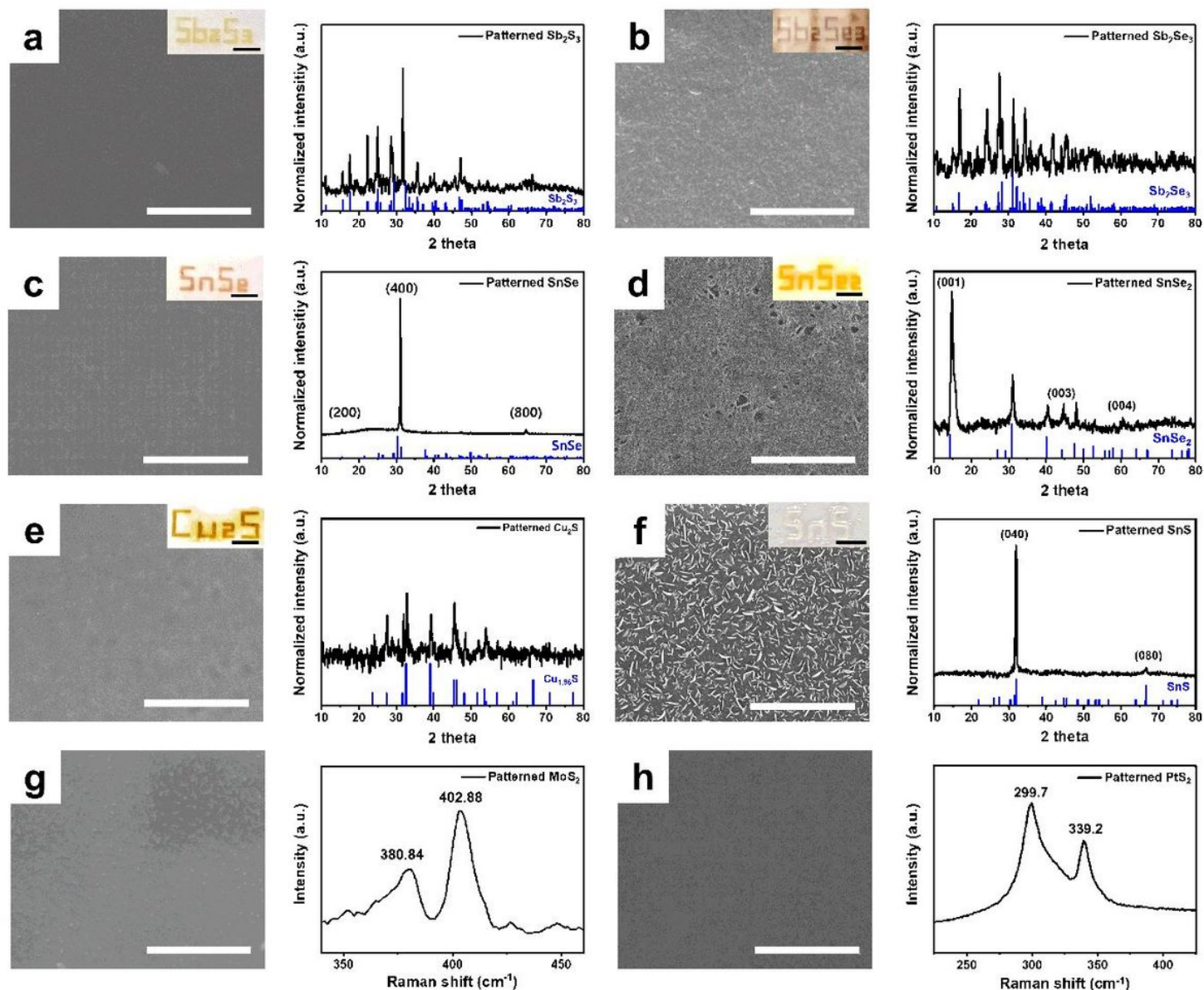


Figure 2

**DLP printing of ChaM-based inks.** **a** SEM image of the printed line patterns of PtS<sub>2</sub>-based ChaM ink with widths ranging from 100  $\mu\text{m}$  to 25  $\mu\text{m}$ . **b** SEM image of the printed circles, squares, and triangles of PtS<sub>2</sub>-based ChaM ink at different scales of tens to hundreds of micrometres. **c** SEM image of hundreds of printed square array patterns with a width of 100  $\mu\text{m}$  at a scale of several millimetres. **d** SEM image of the printed geometric pattern of MoS<sub>2</sub>-based ChaM ink with a linewidth of 50  $\mu\text{m}$  created by the DLP

method. **e** SEM images of the printed maze and its solution line patterned with multiple ChaMs. **f** SEM and 3D scan analysis (inset) images of the printed 3D architecture composed of circle- and triangle-shaped layers. **g** Height profile of the printed 3D architecture. All scale bars in the panels a-f indicate 500  $\mu\text{m}$ .



**Figure 3**

**Microstructures and crystallinity of the printed metal chalcogenides.** SEM images, XRD patterns, and photographs of the printed **a**  $\text{Sb}_2\text{S}_3$ , **b**  $\text{Sb}_2\text{Se}_3$ , **c**  $\text{SnSe}$ , **d**  $\text{SnSe}_2$ , **e**  $\text{Cu}_2\text{S}$ , and **f**  $\text{SnS}$ . SEM images and Raman spectra of **g**  $\text{MoS}_2$  and **h**  $\text{PtS}_2$ . (Scale bars: SEM images: 3  $\mu\text{m}$ , inset images: 5 mm)

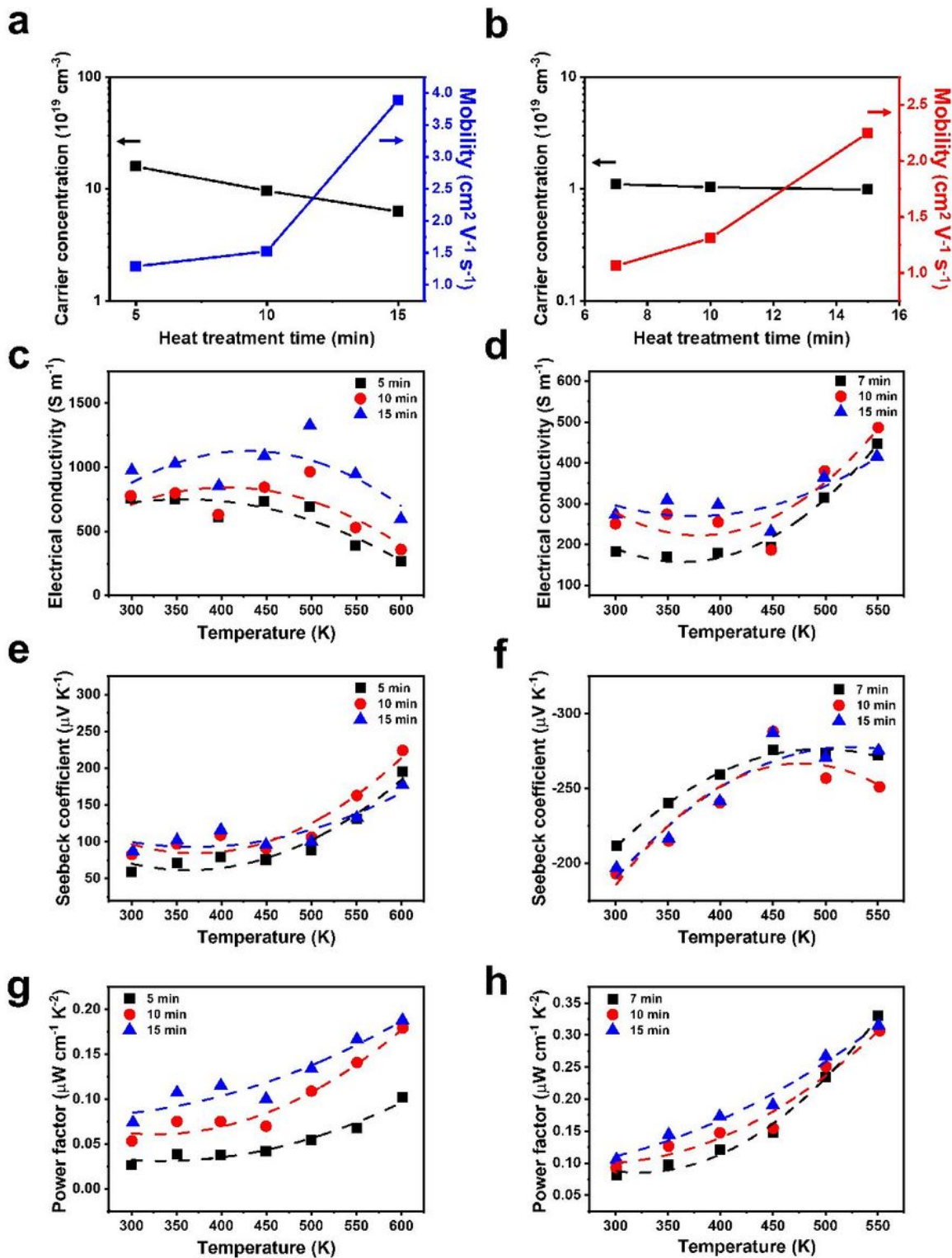


**Figure 4**

**Functionality of the printed metal chalcogenide semiconductors.** Charge carrier mobility and concentration of the printed **a**  $\text{Cu}_2\text{S}$  and **b**  $\text{SnSe}_2$  as functions of the heat treatment time as detected by Hall effect measurements. Temperature dependences of **c**, **d** electrical conductivity, **e**, **f** Seebeck coefficient, and **g**, **h** power factor of the printed  $\text{Cu}_2\text{S}$  (c,e,g) and  $\text{SnSe}_2$  (d,f,h) as functions of the heat treatment time.

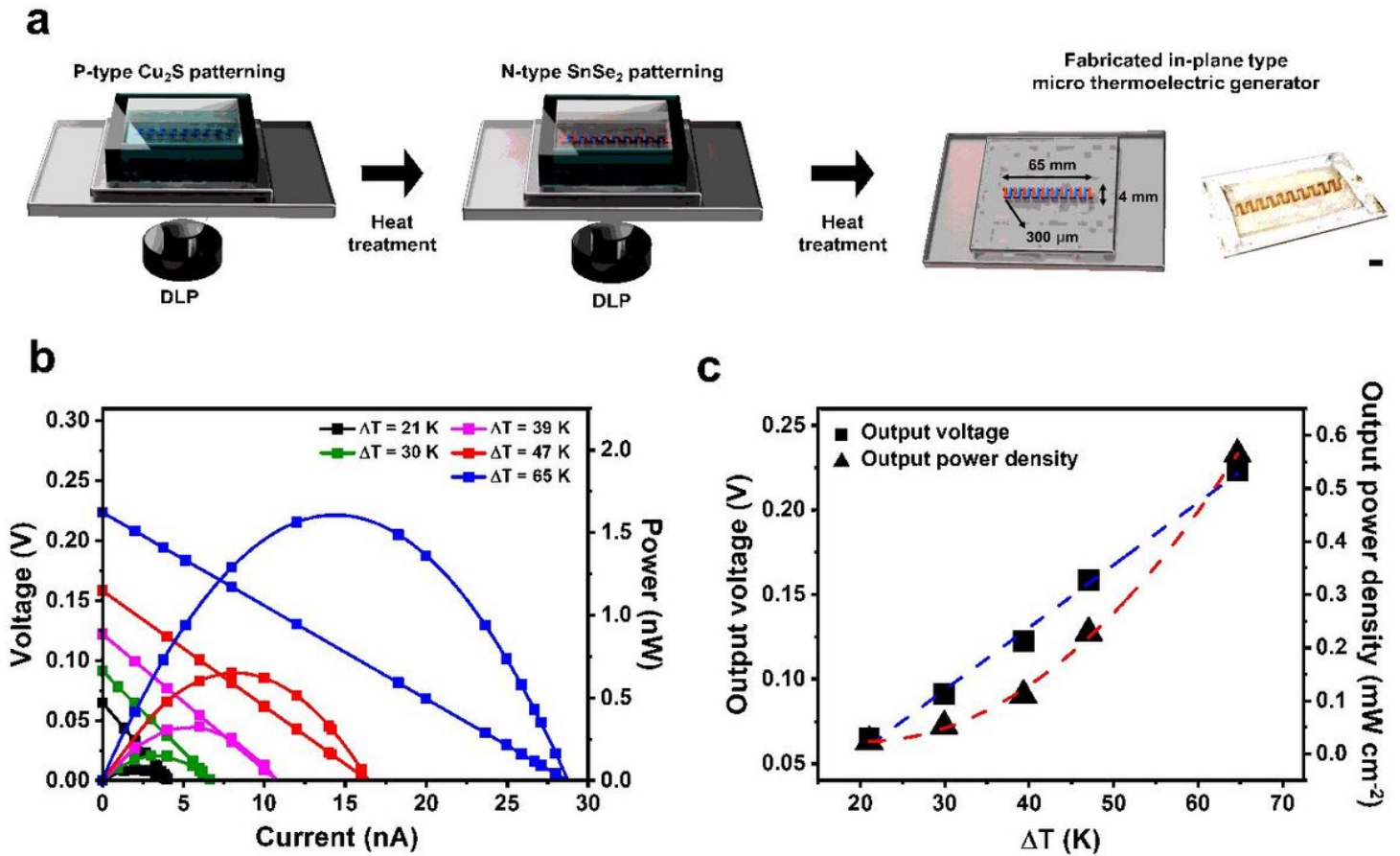


Figure 5

**Fabrication and evaluation of the micro-scale thermoelectric generator.** **a** Scheme of the fabrication of the micro-scale thermoelectric generator by DLP-based optical printing. (Scale bar: 5 mm) **b** Output voltages and powers of the micro-scale thermoelectric generator at various temperature differences. **c** Plots of output voltage and power density as functions of temperature difference.

## Supplementary Files

This is a list of supplementary files associated with this preprint. Click to download.

- [SupplementaryInformation.pdf](#)